Ultrasonics 111 (2021) 106330

Contents lists available at ScienceDirect

Ultrasonics

journal homepage: www.elsevier.com/locate/ultras

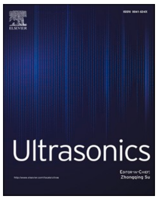

Generalised bisection method for optimum ultrasonic ray tracing and focusing in multi-layered structures

Carmelo Mineo [a,*], David Lines [b], Donatella Cerniglia [a]

[a] *Department of Engineering, University of Palermo, Viale delle Scienze, Edificio 8, 90128 Palermo, Italy*
[b] *Department of Electronic & Electrical Engineering (EEE), University of Strathclyde, 204 George St, Glasgow G1 1XW, UK*

A R T I C L E I N F O

Keywords:
Ultrasonic wave propagation
Ray tracing
Mathematical modelling
Bisection method
Multi-layered structures
Weld inspection
Composites

A B S T R A C T

Ultrasonic testing has been used for many decades, proving itself very efficient for detecting defects in many industrial sectors. The desire to apply ultrasonic testing to geometrically complex structures, and to anisotropic, inhomogeneous materials, together with the advent of more powerful electronics and software, is constantly pushing the applicability of ultrasonic waves to their limits. General ray tracing models, suitable for calculating the proper incident angle of single element probes and the proper time delay of phased array, are currently required. They can support the development of new imaging techniques, as Full Matrix Capture and Total Focusing Method, and the execution of very challenging ultrasonic inspections. This paper introduces a generalized iterative method for the computation of ultrasonic ray paths, when ultrasonic source and target are separated by multiple complex material interfaces in the two dimensional and three dimensional domains. The manuscript starts with a review of the well-known bisection method, and extends the applicability of the method to cases with increasing complexity. An application example, in the field of in-process weld inspection, shows that the introduced generalised bisection method can enable the computation of optimum incidence angles and focal delays for accurate ultrasonic focusing. There is no restriction on the analytical interfaces to be surjective. Interface folding is permitted. It is not necessary to know, a priori, with what sequence the interfaces are crossed by the rays. The presented implementation of the method completes each iteration of the bisection method in 4 ms, for a case with a single interface, and in 960 ms for the case with 52 interfaces.

1. Introduction

Ultrasonic testing (UT) is a family of non-destructive testing techniques based on the propagation of ultrasonic waves in the object or material tested. In most common UT applications, very short ultrasonic pulse-waves with centre frequencies ranging from 0.1 to 15 MHz, and occasionally up to 50 MHz, are transmitted into materials to detect internal flaws or to characterize materials. Ultrasonic testing is often performed on steel, concrete, wood and composites. It is used in many industries including steel and aluminium construction, metallurgy, manufacturing, petrochemical, aerospace, automotive and other transportation sectors [1,2]. UT inspection of planar components is relatively straightforward. However, the inspection of components with nonplanar surface geometries, such as weld-caps, curved pipes, and curved composite structures is more challenging and requires specific technologic solutions. Various works have addressed the inspection of curved components and developed ways to couple the ultrasonic transducers with the material under test, using flexible ultrasonic arrays conforming to the surface [3], deploying a rigid array on a nearby planar surface to image the region of interest from the side either directly [4] or by using signals reflected from the back wall of the component [5]. Another option is to use an intermediary layer (e.g., a solid shoe with a surface conformal with that of the component or water), to couple the transducer to the component [6–8]. However, the imaging speed depends on the complexity of the surface and the total number of image pixels, and this is a key concern for industrial end-users. To increase imaging speed, and improve focusing and/or steering of phased array (PA) ultrasonic beams on the desired position, several works have investigated ways to compute the ultrasonic ray paths [9–11]. One solution is to use the Fast-Marching Method (FMM) combined with Fermat's principle, considering the domain of interest as a grid of connected points, and then use Dijkstra's algorithm [12]. FMM has been extended to heterogeneous materials, where each region can be anisotropic [13]. However, a general ray tracing model based on Snell's law, suitable for calculating the

---

* Corresponding author.
E-mail address: carmelo.mineo01@unipa.it (C. Mineo).

https://doi.org/10.1016/j.ultras.2020.106330
Received 25 August 2020; Received in revised form 21 October 2020; Accepted 2 December 2020

proper incident angle of single element probes and the proper time delay of phased array probes in two and three dimensional multi-layer parts, and in anisotropic and inhomogeneous materials, is still missing. This paper introduces a generalized iterative method for the computation of ultrasonic ray paths, when ultrasonic source and target are separated by multiple complex material interfaces in the two and three dimensional domains. The manuscript starts with a review of the well-known bisection method in Section 2. It then demonstrates the application of the method to cases with increasing complexity (flat material interfaces in Section 3 and curved two dimensional interfaces in Section 4), concluding with the generalisation of the method for its applicability to ray tracing through multiple complex interfaces in the three dimensional domain. The paper discusses application examples and results in Section 6 and draws the conclusions in Section 7.

2. Bisection method

The bisection method is a root-finding method that applies to any continuous functions for which one knows two values with opposite signs [14]. The method consists of repeatedly bisecting the interval defined by these values and then selecting the subinterval in which the function changes sign, and therefore must contain a root. The method is also called the interval halving method [15], the binary search method [14], or the dichotomy method [16].

The method is applicable for numerically solving the equation $f(x) = 0$ for the real variable x, where $f(x)$ is a continuous function defined on an interval $[a, b]$ and where $f(a)$ and $f(b)$ have opposite signs. In this case a and b are said to bracket a root since, by the intermediate value theorem, the continuous function $f(x)$ must have at least one root in the interval (a, b). The interval halving method is an iterative method. At each iteration the method divides the interval in two by computing the midpoint $c = \frac{(a+b)}{2}$ of the interval and the value of the function $f(c)$. Unless c is itself a root (which is very unlikely, but possible), there are only two possibilities: either $f(a)$ and $f(c)$ have opposite signs and bracket a root, or $f(c)$ and $f(b)$ have opposite signs and bracket a root. The method selects the subinterval that is guaranteed to be a bracket as the new interval to be used in the next iteration. Explicitly, if $f(a)$ and $f(c)$ have opposite signs, then the method sets c as the new value for b, and if $f(c)$ and $f(b)$ have opposite signs then the method sets c as the new a. In both cases, the new $f(a)$ and $f(b)$ have opposite signs, so the method is applicable to this smaller interval. In this way, the interval that contains a zero of $f(x)$ is reduced in width by 50% at each iteration. The process is continued until the interval is sufficiently small or if $f(c) = 0$. Then c is taken as the root of the function and the process stops.

3. Flat material interfaces

Given a source of ultrasonic energy in a point S and defining the point T as the target point, where one wants to send the energy, Fig. 1 shows the ultrasonic ray tracing for multiple material layers, in the two dimensional case. Although the figure illustrates the ray tracing for the case of a structure with four material layers, the algorithms presented in this work are generalized for k layers, with k being not predetermined.

Thus, using the notation in Fig. 1a and generalizing for k layers, the following equation is valid:

$$\overline{SP_1^x} + \left(\sum_{i=2}^{k-1}\overline{P_{i-1}^x P_i^x}\right) + \overline{P_{k-1}^x T^x} = \overline{ST^x} \tag{1}$$

Considering that the lengths of the segments on the left-hand side of the equation are equal to the product of the layer thicknesses (d_i) and the tangents of the angles of incidence/refraction (θ_i), in each layer, we have:

$$d_1 \bullet \tan\theta_1 + \left(\sum_{i=2}^{k-1} d_i \bullet \tan\theta_i\right) + d_k \bullet \tan\theta_k = \overline{ST^x} \tag{2}$$

$$d_1 \bullet \tan\theta_1 + \left(\sum_{i=2}^{k} d_i \bullet \tan\theta_i\right) = \overline{ST^x} \tag{3}$$

The relationship between the angles of incidence and refraction, when referring to waves passing through a boundary between two different isotropic media, is described by the Snell's law (also known as Snell-Descartes law and the law of refraction) [17]. The law follows from Fermat's principle of least time [18]. Snell's law states that the ratio of the sines of the angles of incidence and the speed of propagation of the wave is equivalent to the ratio of the sine of the refracted angle and the propagation speed in the media where the wave is refracted. Therefore, the following is valid:

$$\frac{\sin\theta_1}{v_1} = \dots = \frac{\sin\theta_i}{v_i} = \dots = \frac{\sin\theta_k}{v_k} \tag{4}$$

Note that each angle is measured from the normal of the boundary interface and the propagation velocities in the respective media are inserted in the formula in meters per second (m/s). Thus, it is possible to express each angle, θ_i, as a function of the first incidence angle θ_1, and the respective propagation velocities (v_i, v_1):

$$\theta_i = asin\left(\frac{v_i}{v_1} \bullet \sin\theta_1\right) \tag{5}$$

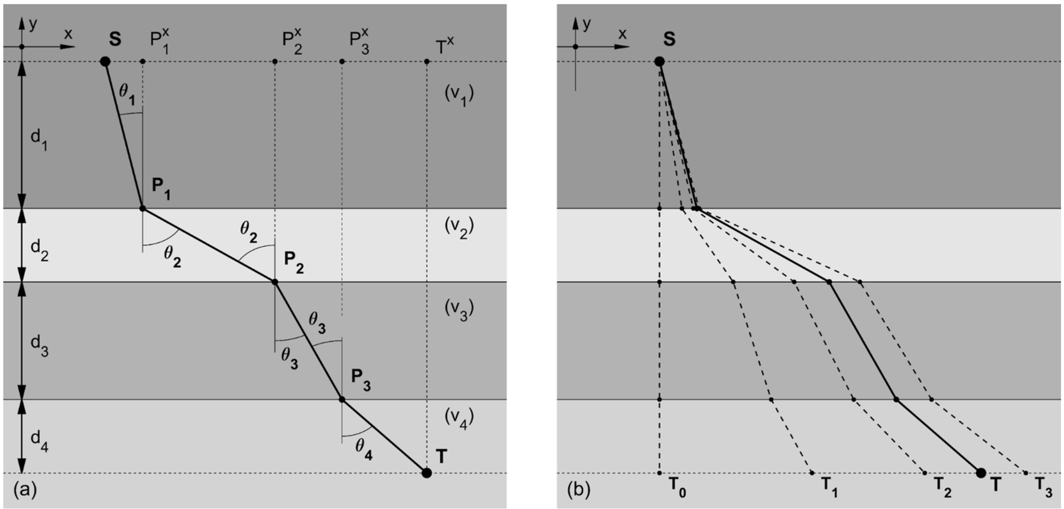

Fig. 1. (a) Annotated ultrasonic ray tracing for multiple material layers in the two dimensional case and (b) convergence to solution through the bisection method.

Replacing Eq. (5) in Eq. (3), we get the following function, $e(\theta_1)$:

$$\begin{aligned} e(\theta_1) &= d_1 \bullet \tan\theta_1 + \left(\sum\nolimits_{i=2}^{k} d_i \bullet \tan\left[asin\left(\frac{v_i}{v_1}\bullet \sin\theta_1\right)\right]\right) - \overline{ST^x} = \\ &= d_1 \bullet \tan\theta_1 + \left(\sum\nolimits_{i=2}^{k} d_i \bullet \frac{v_i \bullet \sin\theta_1}{\sqrt{v_1^2 - v_i^2 \bullet sin^2\theta_1}}\right) - \overline{ST^x} \end{aligned} \tag{6}$$

Therefore, the bisection method is applied to this function. Note the final form of the function, makes use of the identity: $tan[asin(v_i/v_1 \bullet \sin\theta_1)] = (v_i/v_1 \bullet \sin\theta_1)/\sqrt{1-(v_i/v_1 \bullet \sin\theta_1)^2} = (v_i \bullet \sin\theta_1)/\sqrt{v_1^2 - v_i^2 \bullet sin^2\theta_1}$, which is only defined when $v_1^2 - v_i^2 \bullet sin^2\theta_1 > 0$. This leads to determine the interval (a, b) as:

$$\left(asin\left(-\frac{v_1}{\max(v_i)}\right), asin\left(\frac{v_1}{\max(v_i)}\right)\right) \tag{7}$$

$e(\theta_1)$ is a continuous function, in the interval (a, b). Fig. 2 shows the typical shape of the curve associated to $e(\theta_1)$. The curve has been computed for an example multi-layered structure (Fig. 1a) with 4 layers of thicknesses $d_1 = 10$ mm, $d_2 = 5$ mm, $d_3 = 8$ mm and $d_4 = 5$ mm, where the ultrasonic propagation velocities are $v_1 = 1.5$ mm/μs, $v_2 = 6$ mm/μs, $v_3 = 3.1$ mm/μs and $v_4 = 5$ mm/μs, respectively.

The values $e(a)$ and $e(b)$ are of opposite sign. Thus, there is one zero crossing within the interval and the bisection method can be applied. Each iteration of the method performs these steps: (1) the midpoint of the interval $c = \frac{a+b}{2}$ is calculated, (2) the function value at the midpoint $e(c)$ is computed, (3) if convergence is satisfactory (that is, $(c - a)$ and/or $|e(c)|$ sufficiently small), c is returned and the iteration stops; otherwise, the sign of $e(c)$ is examined and either $(a, e(a))$ or $(b, e(b))$ are replaced with $(c, e(c))$, so that there is a zero crossing within the new interval and all steps are repeated. Fig. 1b illustrates the ray tracing relative to the initial guess for the zero of the function $\left(\theta_1^0 = c = \frac{a+b}{2}\right)$, the first three iterations of the method and the final result at the target, for the reference example.

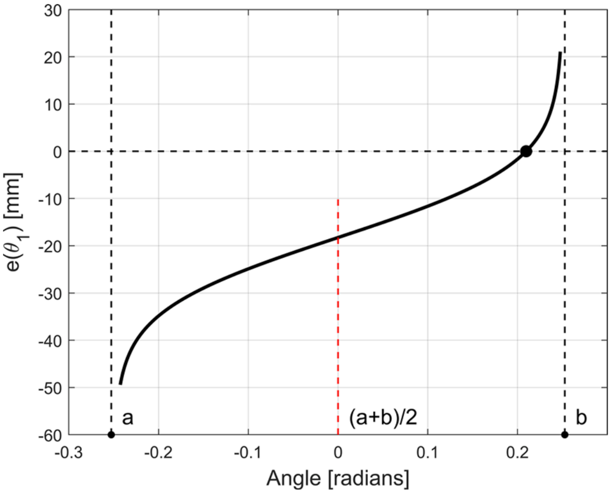

Fig. 2. Typical shape of $e(\theta_1)$.

4. Curved material interfaces (two dimensional case)

Perfectly flat interfaces are only a theoretical abstraction, since real interfaces always present some degree of roughness and deviation from flatness. Moreover, intentionally curved material interfaces are often present in parts that are designed to meet critical mechanical properties. Therefore, it is necessary to generalize the formulation in Section 3, to include the possibility to solve wave propagation through multiple media, separated by curved interfaces (Fig. 3a). Eq. (1) is still valid for this scenario. However, the variable thickness of the material layers does not allow to compute the length of the segments $\overline{SP_1^x}$, $\overline{P_{i-1}^x P_i^x}$ and $\overline{P_{k-1}^x T^x}$ as $d_1 \bullet \tan\theta_1$, $d_i \bullet \tan\theta_i$ and $d_k \bullet \tan\theta_k$ respectively. Instead, introducing the function $f_1(x)$ to describe the curved interface between the first and second layer, the first incidence point, $P_1 \equiv (P_1^x, P_1^y)$, can be found through intersecting the propagation line in the first layer with the first interface $f_1(x)$.

Therefore, P_1^x and P_1^y are the solution of the system containing the equation of the line for the source S and the equation relative to the first interface, $y = f_1(x)$, as illustrated in Eq. (8).

$$\begin{aligned} &\text{if } \theta_1 \neq 0 \\ &\quad \begin{cases} line\ \ for\ \ S: & y = tan\left(\frac{\pi}{2} + \theta_1\right) \bullet (x - S^x) - S^y \\ first\ \ interface: & y = f_1(x) \end{cases} \\ &\text{else} \\ &\quad \begin{cases} line\ \ for\ \ S: & x = S^x \\ first\ \ interface: & y = f_1(S^x) \end{cases} \\ &\text{end} \end{aligned} \tag{8}$$

Throughout this paper, the assumption is that each interface surface is smooth and continuous with a local radius of curvature that is many times greater than the ultrasonic wavelength. Under these conditions, a ray-based approach is valid and the problem becomes one of computing the correct ray path between source positions and target within the component. Fig. 4a illustrates the refraction of an incidence wave at point P_1, on the first interface.

Whereas θ_1 and θ_2 are the angles that incidence and refracted wave form with the y-axis, α_1 and α_2 are the respective angles formed with the normal to the interface at the incidence point P_1. These latter angles are constrained by the Snell's law and obey to the following equation:

$$\frac{\sin\alpha_1}{v_1} = \frac{\sin\alpha_2}{v_2} = \cdots = \frac{\sin\alpha_i}{v_i} = \frac{\sin\alpha_k}{v_k} \tag{9}$$

From Fig. 4a, it is evident that:

$$\alpha_1 = \theta_1 - \text{atan}\left(f_1'(P_1^x)\right) \tag{10}$$

$$\alpha_2 = \theta_2 - \text{atan}\left(f_1'(P_1^x)\right) \tag{11}$$

Replacing Eqs. (10) and (11) in Eq. (9), it results:

$$\theta_2 = asin\left\{\left(\frac{v_2}{v_1}\right) \bullet \sin\left[\theta_1 - atan\left(f_1'(P_1^x)\right)\right]\right\} + atan\left(f_1'(P_1^x)\right) \tag{12}$$

and generalising for the i^{th} angle (θ_i) at the i^{th} layer, and for the k^{th} angle (θ_k) at the last layer:

$$\theta_i = asin\left\{\left(\frac{v_i}{v_1}\right) \bullet \sin\left[\theta_1 - atan\left(f_1'(P_1^x)\right)\right]\right\} + atan\left(f_{i-1}'(P_{i-1}^x)\right) \tag{13}$$

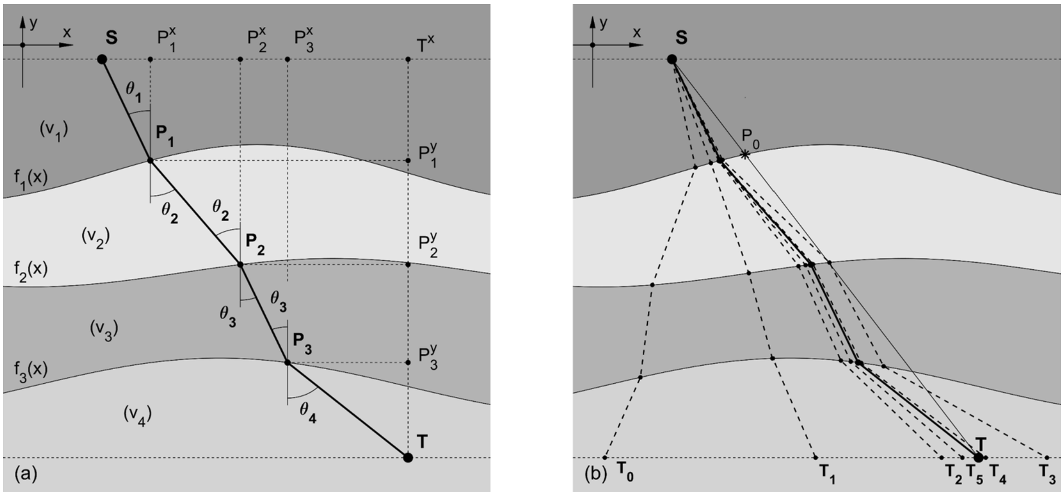

Fig. 3. Annotated ultrasonic ray tracing for multiple material layers separated by curved interfaces (a) and convergence to solution through the bisection method (b).

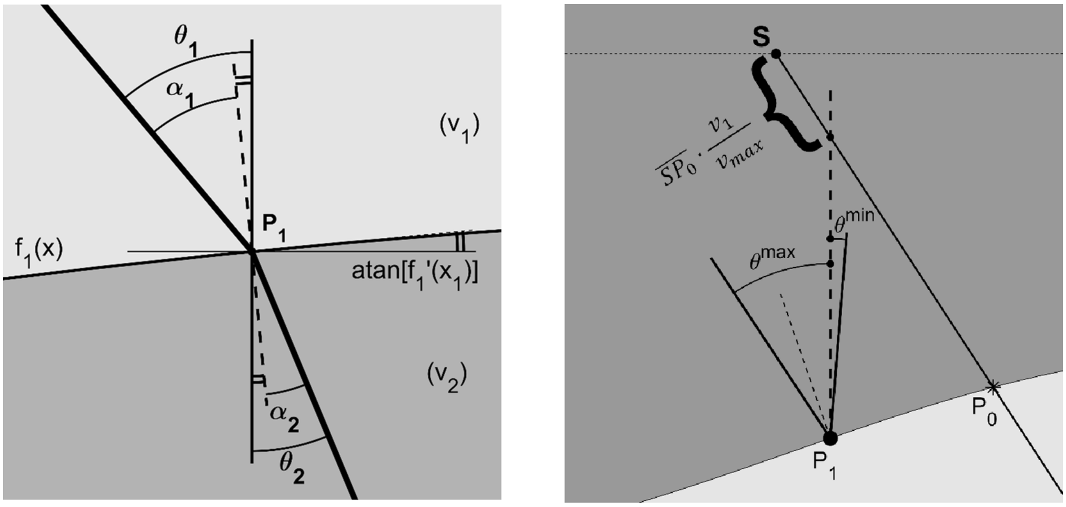

(a) (b)

Fig. 4. (a) Refraction at point $\boldsymbol{P}_1$, on the first material interface and (b) approach used for defining the initial guess point and the domain interval for $\boldsymbol{\theta}_1$.

$$\theta_k = asin\left\{\left(\frac{v_k}{v_1}\right)\cdot\sin\left[\theta_1 - atan\left(f_1^{'}\left(P_1^x\right)\right)\right]\right\} + atan\left(f_{k-1}^{'}\left(P_{k-1}^x\right)\right) \tag{14}$$

Therefore, the coordinates (P_i^x, P_i^y) of the incidence points, from the 2nd to the $(k-1)^{\text{th}}$ incidence points, are the solution of the system with the equation of the line for the source P_{i-1} and the equation relative to the i^{th} interface, $y = f_i(x)$, as illustrated in Eq. (15).

```
for i = 2 : (k − 1)
    $\theta_i = asin\left\{\left(\frac{v_i}{v_1}\right)\cdot\sin\left[\theta_1 - atan\left(f_1^{'}\left(P_1^x\right)\right)\right]\right\} + atan\left(f_{i-1}^{'}\left(P_{i-1}^x\right)\right)$
    if $\theta_i \neq 0$
        $\begin{cases} line\ for\ P_{i-1}: & y = tan\left(\frac{\pi}{2}+\theta_i\right)\cdot\left(x - P_{i-1}^x\right) - P_{i-1}^y \\ i^{th}\ interface: & y = f_i(x) \end{cases}$        (15)
    else
        $\begin{cases} line\ for\ P_{i-1}: & x = P_{i-1}^x \\ i^{th}\ interface: & y = f_i\left(P_{i-1}^x\right) \end{cases}$
    end
end
```

Finally, the coordinates $\left(T_0^x, T_0^y\right)$ of the resulting target point related to the initial guess angle θ_1 (given as input), are the solution of the system with the equation of the line for the point P_{k-1} and the horizontal line for T ($y = T^y$), as shown in Eq. (16).

$$\theta_k = asin\left\{\left(\frac{v_k}{v_1}\right)\cdot\sin\left[\theta_1 - atan\left(f_1^{'}\left(P_1^x\right)\right)\right]\right\} + atan\left(f_{k-1}^{'}\left(P_{k-1}^x\right)\right)$$

$$\text{if } \theta_k \neq 0$$

$$\begin{cases} line\ for\ P_{k-1}: & x = P_{k-1}^x + \left(P_{k-1}^y - T^y\right)\cdot tan(\theta_k) \\ horiz.lineforT: & y = T^y \end{cases} \tag{16}$$

$$\text{else}$$

$$\begin{cases} line\ for\ P_{k-1}: & x = P_{k-1}^x \\ horiz.line\ for\ T: & y = T^y \end{cases}$$

$$\text{end}$$

Thus, the bisection method is applied to the error function, $e(\theta_1)$, defined as:

$$e(\theta_1) = \overline{T_jT} = T^x - T_j^x \tag{17}$$

The identification of the correct domain for $e(\theta_1)$ is crucial to make sure the application of the bisection method leads to convergence. Eqs. (13) and (14) are only defined where $-1 < \left(\frac{v_i}{v_1}\right)\cdot\sin\left[\theta_1 - atan\left(f_1^{'}\left(P_1^x\right)\right)\right]\langle 1$. This leads to determine the interval (a, b) as:

$$(a,b) = \left(\theta^{min}, \theta^{max}\right) = \left(asin\left(-\frac{v_1}{\max(v)}\right) + atan\left(f_1^{'}\left(P_1^x\right)\right), asin\left(\frac{v_1}{\max(v)}\right) + atan\left(f_1^{'}\left(P_1^x\right)\right)\right) \tag{18}$$

It is clear that the extremities of the interval depend on the incidence point at the first interface, since the derivative of $f_1(x)$ is computed for $x = P_1^x$ in Eq. (18). In this work, the intersection between the segment $\overline{ST}$ and the first interface $f_1(x)$ is used to guide the selection of such initial guess point. Indicating with $P_0 \equiv \left(P_0^x, P_0^y\right)$ the intersection between $\overline{ST}$ and $f_1(x)$, the initial guess point is chosen as: $P_1 \equiv \left(P_1^x, P_1^y\right) \equiv \left(S^x + \frac{v_1}{v_{max}}\cdot\left(P_0^x - S^x\right), f_1\left(S^x + \frac{v_1}{v_{max}}\cdot\left(P_0^x - S^x\right)\right)\right)$, as it is illustrated in Fig. 4b. The function values $e(a)$ and $e(b)$ are of opposite sign and there is one zero crossing within the interval. Therefore, the bisection method can be applied, following the same steps as for the case with flat interfaces until convergence is satisfactory (that is, $(c - a)$ and/or $|e(c)|$ sufficiently small), returning c and stopping iterating. Fig. 3b illustrates the ray tracing relative to the initial guess $\left(\theta_1^0 = \frac{a+b}{2}\right)$, the first five iterations of the method and the final result at the target.

5. Curved material interfaces (three dimensional case)

The propagation of a wave through a number (k) of material layers, separated by curved interfaces in the three dimensional case, is the more general situation (Fig. 5). Indeed, the previous two dimensional problem can be solved as particular case of this general case. The modelling of the three dimensional problem is the main contribution of this work.

Introducing the function $f_1(x, y)$ to describe the curved interface surface between the first and second layer, the first incidence point, $P_1 \equiv \left(P_1^x, P_1^y, P_1^z\right)$, is the solution of the system with the Cartesian representation of the line for the source S and the equation relative to the first interface, $z = f_1(x, y)$. In the three dimensional case it is easier to describe the direction of incidence through the unitary vector $\overrightarrow{r}_1 = \langle r_1^x, r_1^y, r_1^z\rangle$, rather than an angle θ_1. Therefore, the coordinates of the incidence point (P_1), resulting from the system illustrated, are given in Eq. (19).

$$\text{if}\left(r_1^x \neq 0, r_1^y \neq 0, r_1^z \neq 0\right)$$

$$\begin{cases} line\ for\ S: & \begin{cases} \dfrac{x - S^x}{r_1^x} = \dfrac{y - S^y}{r_1^y} \\ \dfrac{y - S^y}{r_1^y} = \dfrac{z - S^z}{r_1^z} \end{cases} \\ first\ interface: & z = f_1(x, y) \end{cases}$$

$$\text{elseif}\left(r_1^x = 0, r_1^y \neq 0, r_1^z \neq 0\right)$$

$$\begin{cases} line\ for\ S: & \begin{cases} x = S^x \\ \dfrac{y - S^y}{r_1^y} = \dfrac{z - S^z}{r_1^z} \end{cases} \\ first\ interface: & z = f_1(x, y) \end{cases}$$

$$\text{elseif}\left(r_1^x \neq 0, r_1^y = 0, r_1^z \neq 0\right)$$

$$\begin{cases} lineforS: & \begin{cases} y = S^y \\ \dfrac{x - S^x}{r_1^x} = \dfrac{z - S^z}{r_1^z} \end{cases} \\ firstinterface: & z = f_1(x, y) \end{cases}$$

$$\text{elseif}\left(r_1^x \neq 0, r_1^y \neq 0, r_1^z = 0\right)$$

$$\begin{cases} line\ for\ S: & \begin{cases} z = S^z \\ \dfrac{x - S^x}{r_1^x} = \dfrac{y - S^y}{r_1^y} \end{cases} \\ first\ interface: & z = f_1(x, y) \end{cases} \tag{19}$$

$$\text{elseif}\left(r_1^x = 0, r_1^y = 0, r_1^z \neq 0\right)$$

$$\begin{cases} line\ for\ S: & \begin{cases} x = S^x \\ y = S^y \end{cases} \\ first\ interface: & z = f_1(x, y) \end{cases}$$

$$\text{elseif}\left(r_1^x = 0, r_1^y \neq 0, r_1^z = 0\right)$$

$$\begin{cases} line\ for\ S: & \begin{cases} x = S^x \\ z = S^z \end{cases} \\ first\ interface: & z = f_1(x, y) \end{cases}$$

$$\text{elseif}\left(r_1^x \neq 0, r_1^y = 0, r_1^z = 0\right)$$

$$\begin{cases} line\ for\ S: & \begin{cases} y = S^y \\ z = S^z \end{cases} \\ first\ interface: & z = f_1(x, y) \end{cases}$$

$$\text{end}$$

Rewriting the equation relative to the first interface, $z = f_1(x, y)$, as $f_1(x, y, z) = 0$, the unit normal vector to the surface at the point P_1 is given by $\overrightarrow{\boldsymbol{n}}_1 = \nabla \boldsymbol{f}_1(P_1)/\|\nabla \boldsymbol{f}_1(P_1)\|$.

$$\overrightarrow{\boldsymbol{n}}_1 = \frac{\nabla \boldsymbol{f}_1(P_1)}{\|\nabla \boldsymbol{f}_1(P_1)\|} = \frac{\left\langle \frac{\partial f_1}{\partial x}\left(P_1^x, P_1^y, P_1^z\right), \frac{\partial f_1}{\partial y}\left(P_1^x, P_1^y, P_1^z\right), \frac{\partial f_1}{\partial z}\left(P_1^x, P_1^y, P_1^z\right)\right\rangle}{\sqrt{\frac{\partial f_1}{\partial x}\left(P_1^x, P_1^y, P_1^z\right)^2 + \frac{\partial f_1}{\partial y}\left(P_1^x, P_1^y, P_1^z\right)^2 + \frac{\partial f_1}{\partial z}\left(P_1^x, P_1^y, P_1^z\right)^2}} = \langle n_1^x, n_1^y, n_1^z \rangle \tag{20}$$

Considering the refraction at the first interface, the unitary vector for the direction ($\overrightarrow{\boldsymbol{r}}_2$) of the refracted wave in the second layer lies in the plane π_1, which also contains the vectors $\overrightarrow{\boldsymbol{r}}_1$ and $\overrightarrow{\boldsymbol{n}}_1$. Fig. 6 introduces the notation of the geometric entities used to compute the refraction direction.

The plane ω_1 is the horizontal plane that passes through P_1 and has normal vector $[0 \quad 0 \quad 1]^T$, which is the plane described by the equation: $z = f_1(P_1)$. The plane τ_1 *is* the plane tangent to the surface $f_1(x, y, z) = 0$ in P_1, whose normal coincides with $\overrightarrow{\boldsymbol{n}}_1$. The direction resulting from the intersection between π_1 and ω_1 is indicated by the unitary vector $\overrightarrow{\boldsymbol{o}}_1$. Instead, $\overrightarrow{\boldsymbol{t}}_1$ is the unitary vector resulting from the intersection between π_1 and τ_1. Finally, the unitary vector perpendicular to π_1 is indicated with $\overrightarrow{\boldsymbol{s}}_1$ and the vector perpendicular to $\overrightarrow{\boldsymbol{s}}_1$ and $\overrightarrow{\boldsymbol{o}}_1$ is designated by $\overrightarrow{\boldsymbol{u}}_1$. Mathematically, the components of these vectors are computed through the following equations:

$$\overrightarrow{\boldsymbol{s}}_1 = \overrightarrow{\boldsymbol{n}}_1 \times \overrightarrow{\boldsymbol{r}}_1 = \begin{pmatrix} r_1^z n_1^y - r_1^y n_1^z \\ r_1^x n_1^z - r_1^z n_1^x \\ r_1^y n_1^x - r_1^x n_1^y \end{pmatrix} = \begin{pmatrix} s_1^x \\ s_1^y \\ s_1^z \end{pmatrix} \tag{21}$$

$$\overrightarrow{\boldsymbol{o}}_1 = \begin{pmatrix} 0 \\ 0 \\ 1 \end{pmatrix} \times \overrightarrow{\boldsymbol{s}}_1 = \begin{pmatrix} r_1^z n_1^x - r_1^x n_1^z \\ r_1^z n_1^y - r_1^y n_1^z \\ 0 \end{pmatrix} = \begin{pmatrix} o_1^x \\ o_1^y \\ o_1^z \end{pmatrix} \tag{22}$$

$$\overrightarrow{\boldsymbol{t}}_1 = \overrightarrow{\boldsymbol{s}}_1 \times \overrightarrow{\boldsymbol{n}}_1 = \begin{pmatrix} n_1^z\left(r_1^x n_1^z - r_1^z n_1^x\right) - n_1^y\left(r_1^y n_1^x - r_1^x n_1^y\right) \\ n_1^x\left(r_1^y n_1^x - r_1^x n_1^y\right) - n_1^z\left(r_1^z n_1^y - r_1^y n_1^z\right) \\ n_1^y\left(r_1^z n_1^y - r_1^y n_1^z\right) - n_1^x\left(r_1^x n_1^z - r_1^z n_1^x\right) \end{pmatrix} = \begin{pmatrix} t_1^x \\ t_1^y \\ t_1^z \end{pmatrix} \tag{23}$$

$$\overrightarrow{\boldsymbol{u}}_1 = \overrightarrow{\boldsymbol{s}}_1 \times \overrightarrow{\boldsymbol{o}}_1 = \begin{pmatrix} \left(r_1^x n_1^y - r_1^y n_1^x\right)\left(r_1^z n_1^y - r_1^y n_1^z\right) \\ \left(r_1^y n_1^x - r_1^x n_1^y\right)\left(r_1^z n_1^x - r_1^x n_1^z\right) \\ \left(r_1^z n_1^y - r_1^y n_1^z\right)^2 + \left(r_1^x n_1^z - r_1^z n_1^x\right)^2 \end{pmatrix} = \begin{pmatrix} u_1^x \\ u_1^y \\ u_1^z \end{pmatrix} \tag{24}$$

Therefore, it is possible to define the rotational matrix $\boldsymbol{R}_1$, which is used to transform the vectors $\overrightarrow{\boldsymbol{r}}_1$, $\overrightarrow{\boldsymbol{n}}_1$ and $\overrightarrow{\boldsymbol{t}}_1$ in the rotated vectors $\overrightarrow{\boldsymbol{r}}_1^{'}$, $\overrightarrow{\boldsymbol{n}}_1^{'}$ and $\overrightarrow{\boldsymbol{t}}_1^{'}$.

$$\boldsymbol{R}_1 = \left[\overrightarrow{\boldsymbol{o}}_1 \overrightarrow{\boldsymbol{u}}_1 \overrightarrow{\boldsymbol{s}}_1\right] = \begin{bmatrix} o_1^x & u_1^x & s_1^x \\ o_1^y & u_1^y & s_1^y \\ o_1^z & u_1^z & s_1^z \end{bmatrix} \tag{25}$$

$$\overrightarrow{\boldsymbol{r}}_1^{'} = \overrightarrow{\boldsymbol{r}}_1 \cdot \boldsymbol{R}_1 = \begin{pmatrix} r_1^x \\ r_1^y \\ r_1^z \end{pmatrix}^T \cdot \begin{bmatrix} o_1^x & u_1^x & s_1^x \\ o_1^y & u_1^y & s_1^y \\ o_1^z & u_1^z & s_1^z \end{bmatrix} = \begin{pmatrix} r_1^x o_1^x + r_1^y o_1^y + r_1^z o_1^z \\ r_1^x u_1^x + r_1^y u_1^y + r_1^z u_1^z \\ r_1^x s_1^x + r_1^y s_1^y + r_1^z s_1^z \end{pmatrix} = \begin{pmatrix} r_1^{x'} \\ r_1^{y'} \\ r_1^{z'} \end{pmatrix} = \tag{26}$$

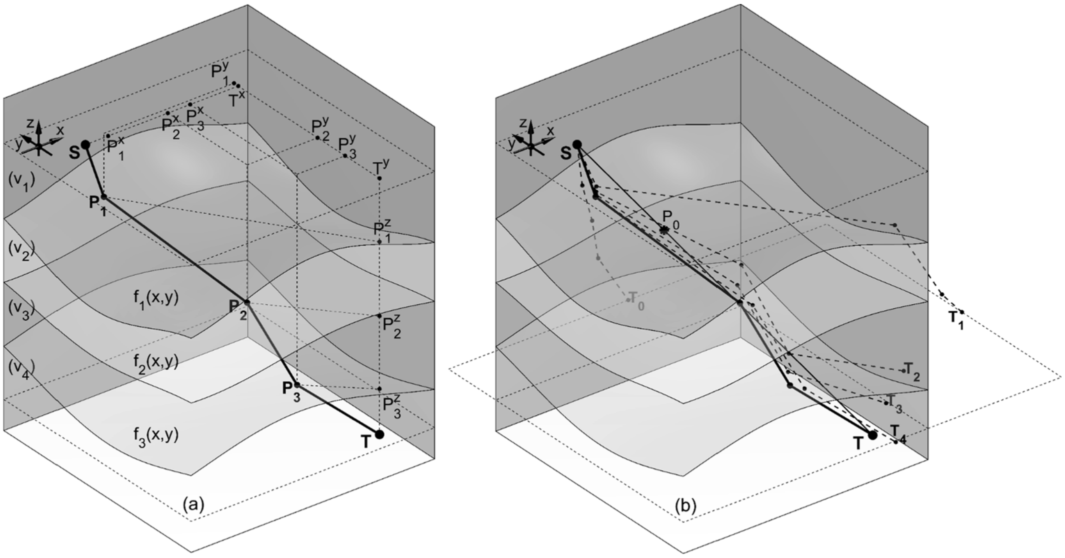

Fig. 5. Annotated ultrasonic ray tracing for multiple material layers separated by curved interfaces in the three dimensional case (a) and convergence to solution through the bisection method (b).

$$= \begin{pmatrix} r_1^x r_1^z n_1^x - \left(r_1^x\right)^2 n_1^z + r_1^y r_1^z n_1^y - (r_1^y)^2 n_1^z \\ \left(r_1^x\right)^2 r_1^z (n_1^y)^2 - 2 r_1^x r_1^y r_1^z n_1^x n_1^y + (r_1^y)^2 r_1^z \left(n_1^x\right)^2 + \left(r_1^z\right)^3 (n_1^y)^2 - 2 r_1^y \left(r_1^z\right)^2 n_1^y n_1^z + (r_1^y)^2 r_1^z \left(n_1^z\right)^2 + \left(r_1^x\right)^2 r_1^z \left(n_1^z\right)^2 - 2 r_1^x \left(r_1^z\right)^2 n_1^x n_1^z + \left(r_1^z\right)^3 \left(n_1^x\right)^2 \\ 0 \end{pmatrix}$$

$$\vec{\boldsymbol{n}}'_1 = \vec{\boldsymbol{n}}_1 \cdot \boldsymbol{R}_1 = \begin{pmatrix} n_1^x \\ n_1^y \\ n_1^z \end{pmatrix}^T \cdot \begin{bmatrix} o_1^x & u_1^x & s_1^x \\ o_1^y & u_1^y & s_1^y \\ o_1^z & u_1^z & s_1^z \end{bmatrix} = \begin{pmatrix} n_1^x o_1^x + n_1^y o_1^y + n_1^z o_1^z \\ n_1^x u_1^x + n_1^y u_1^y + n_1^z u_1^z \\ n_1^x s_1^x + n_1^y s_1^y + n_1^z s_1^z \end{pmatrix} = \begin{pmatrix} n_1^{x'} \\ n_1^{y'} \\ n_1^{z'} \end{pmatrix} = \tag{27}$$

$$= \begin{pmatrix} r_1^z \left(n_1^x\right)^2 - r_1^x n_1^x n_1^z - r_1^y n_1^y n_1^z + r_1^z (n_1^y)^2 \\ \left(r_1^x\right)^2 (n_1^y)^2 n_1^z - 2 r_1^x r_1^y n_1^x n_1^y n_1^z + \left(r_1^y\right)^2 \left(n_1^x\right)^2 n_1^z + \left(r_1^z\right)^2 (n_1^y)^2 n_1^z - 2 r_1^y r_1^z n_1^y \left(n_1^z\right)^2 + (r_1^y)^2 \left(n_1^z\right)^3 + \left(r_1^x\right)^2 \left(n_1^z\right)^3 - 2 r_1^x r_1^z n_1^x \left(n_1^z\right)^2 + \left(r_1^z\right)^2 \left(n_1^x\right)^2 n_1^z \\ 0 \end{pmatrix}$$

$$\vec{\boldsymbol{t}}'_1 = \vec{\boldsymbol{t}}_1 \cdot \boldsymbol{R}_1 = \begin{pmatrix} t_1^x \\ t_1^y \\ t_1^z \end{pmatrix}^T \cdot \begin{bmatrix} o_1^x & u_1^x & s_1^x \\ o_1^y & u_1^y & s_1^y \\ o_1^z & u_1^z & s_1^z \end{bmatrix} = \begin{pmatrix} t_1^x o_1^x + t_1^y o_1^y + t_1^z o_1^z \\ t_1^x u_1^x + t_1^y u_1^y + t_1^z u_1^z \\ t_1^x s_1^x + t_1^y s_1^y + t_1^z s_1^z \end{pmatrix} = \begin{pmatrix} t_1^{x'} \\ t_1^{y'} \\ t_1^{z'} \end{pmatrix} = \tag{28}$$

$$= \begin{pmatrix} -\left(r_1^x\right)^2 (n_1^y)^2 n_1^z + 2 r_1^x r_1^y n_1^x n_1^y n_1^z - (r_1^y)^2 \left(n_1^x\right)^2 n_1^z - \left(r_1^z\right)^2 (n_1^y)^2 n_1^z + 2 r_1^y r_1^z n_1^y \left(n_1^z\right)^2 - (r_1^y)^2 \left(n_1^z\right)^3 - \left(r_1^x\right)^2 \left(n_1^z\right)^3 + 2 r_1^x r_1^z n_1^x \left(n_1^z\right)^2 - \left(r_1^z\right)^2 \left(n_1^x\right)^2 n_1^z \\ r_1^z \left(n_1^x\right)^2 - r_1^x n_1^x n_1^z - r_1^y n_1^y n_1^z + r_1^z (n_1^y)^2 \\ 0 \end{pmatrix}$$

Since $r_1^{z'} = n_1^{z'} = t_1^{z'} = 0$, the rotated vectors can be represented on the $x'y'$-plane, where the imposition of Snell's law is brought back to the two dimensional domain, as illustrated in Fig. 6b. Beside the sign, the angle formed by $\vec{\boldsymbol{t}}'_1$ with the x'-axis is equal to the angle formed by $\vec{\boldsymbol{n}}'_i$ with the y'-axis. Thus, this angle is indicated with $\gamma_1 = atan\left(t_1^{y'}/t_1^{x'}\right) = -atan\left(n_1^{x'}/n_1^{y'}\right)$. Therefore, rewriting Eqs. (13) and (14), which originate from Snell's law, using γ_1 in place of $atan\left(f'_1\left(P_1^x\right)\right)$, the angle formed by the rotated refracted vector ($\vec{\boldsymbol{r}}'_1$) with the y'-axis results:

$$\theta_2 = asin\left\{\left(\frac{v_2}{v_1}\right) \cdot \sin\left[\theta_1 + atan\left(\frac{n_1^{x'}}{n_1^{y'}}\right)\right]\right\} - atan\left(\frac{n_1^{x'}}{n_1^{y'}}\right), \quad \text{with}: \theta_1 = -atan\left(\frac{r_1^{x'}}{r_1^{y'}}\right) \tag{29}$$

Thus, the components of the unitary vector $\vec{\boldsymbol{r}}'_2$ in the two dimensional domain and the components of $\vec{\boldsymbol{r}}_2$ in the original three dimensional space are respectively:

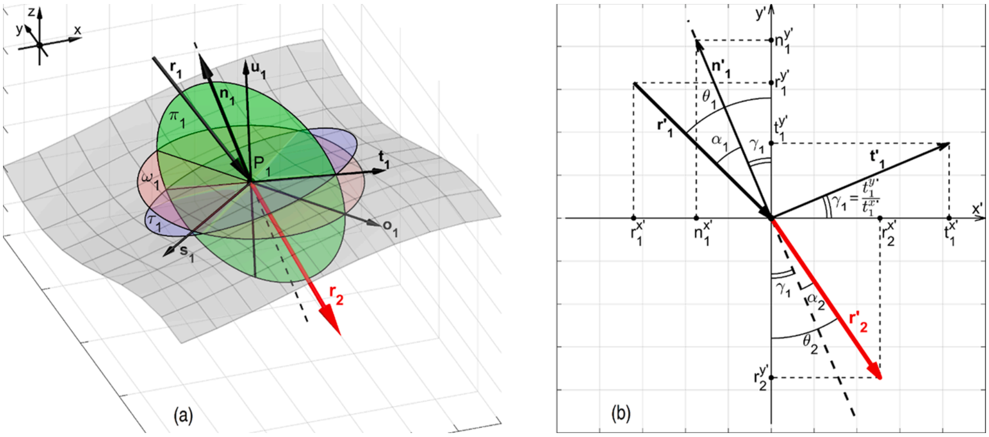

Fig. 6. (a) Refraction in three dimensional space and (b) projection onto the plane x'-y' ($\boldsymbol{\pi}_1$).

$$\overrightarrow{\boldsymbol{r}}'_2 = \begin{pmatrix} r_2^{x'} \\ r_2^{y'} \end{pmatrix} = \begin{pmatrix} \sin(\theta_2) \\ -\cos(\theta_2) \end{pmatrix} \tag{30}$$

$$\overrightarrow{\boldsymbol{r}}_2 = \begin{pmatrix} r_2^{x'} \\ r_2^{y'} \\ 0 \end{pmatrix}^T \cdot \boldsymbol{R}^{-1} = \begin{pmatrix} \sin(\theta_2) \\ -\cos(\theta_2) \\ 0 \end{pmatrix}^T \cdot \begin{bmatrix} o_1^x & u_1^x & s_1^x \\ o_1^y & u_1^y & s_1^y \\ o_1^z & u_1^z & s_1^z \end{bmatrix}^{-1} = \begin{pmatrix} \sin(\theta_2)o_1^x - \cos(\theta_2)o_1^y \\ \sin(\theta_2)u_1^x - \cos(\theta_2)u_1^y \\ \sin(\theta_2)s_1^x - \cos(\theta_2)s_1^y \end{pmatrix} \tag{31}$$

Generalising for the refracted direction in any i^{th} layer $\left(\overrightarrow{\boldsymbol{r}}_{\mathrm{I}}\right)$ and in the last layer $\left(\overrightarrow{\boldsymbol{r}}_k\right)$:

$$\overrightarrow{r}_i = \begin{pmatrix} \sin(\theta_i)o_{i-1}^x - \cos(\theta_i)o_{i-1}^y \\ \sin(\theta_i)u_{i-1}^x - \cos(\theta_i)u_{i-1}^y \\ \sin(\theta_i)s_{i-1}^x - \cos(\theta_i)s_{i-1}^y \end{pmatrix}, \quad \text{with} : \theta_i$$
$$= asin\left\{\left(\frac{v_i}{v_1}\right)\cdot\sin\left[\theta_1 + atan\left(\frac{n_1^{x'}}{n_1^{y'}}\right)\right]\right\} - atan\left(\frac{n_{i-1}^{x'}}{n_{i-1}^{y'}}\right) \tag{32}$$

$e_x\left(\overrightarrow{\boldsymbol{r}}_1\right)$ and $e_y\left(\overrightarrow{\boldsymbol{r}}_1\right)$, defined as:

$$e_x\left(\overrightarrow{\boldsymbol{r}}_1\right) = T^x - T_j^x e_y\left(\overrightarrow{\boldsymbol{r}}_1\right) = T^y - T_j^y \tag{34}$$

As in the two dimensional case, it is crucial to determine the limits of the domain of these error functions to make sure the application of the bisection method leads to convergence. This means defining the interval for the components of the vector $\overrightarrow{\boldsymbol{r}}_1 = \langle r_1^x, r_1^y, r_1^z \rangle$. As $\theta_1 = -atan\left(r_1^{x'}/r_1^{y'}\right)$, Eqs. (32) and (33) are only defined where $-1 < \left(\frac{v_i}{v_1}\right)\cdot sin\left[-atan\left(r_1^{x'}/r_1^{y'}\right) + atan\left(n_1^{x'}/n_1^{y'}\right)\right]\langle 1$. The following system brings together this latter condition and imposes the unitary modulus.

Unfortunately, after replacing $r_1^{x'}$, $r_1^{y'}$, $n_1^{x'}$ and $n_1^{y'}$ with their respective expressions from Eqs. (26) and (27), which are functions of the sought values r_1^x, r_1^y and r_1^z, it is not easy to isolate their domain intervals. In this work an alternative route is found and the domain intervals are approximated by building on the formulation for the two dimensional case. The first two inequalities in the following system derive from the first inequality in Eq. (35), respectively written for the x-z plane and the y-z plane, where the ratio $n_1^{x'}/n_1^{y'}$ is replaced with the partial derivatives of the first interface function for x and y (computed in P_1).

$$\begin{cases} -1 < \left(\dfrac{v_i}{v_1}\right)\cdot sin\left[-atan\left(\dfrac{r_1^{x'}}{r_1^{y'}}\right) + atan\left(\dfrac{n_1^{x'}}{n_1^{y'}}\right)\right]\Bigg\langle 1 \\ \\ \|\overrightarrow{r}_1\| = 0 \end{cases}$$

$$\begin{cases} -1 < \left(\dfrac{v_i}{v_1}\right)\cdot\sin\left[-atan\left(\dfrac{r_1^x r_1^z n_1^x - \left(r_1^x\right)^2 n_1^z + r_1^y r_1^z n_1^y - \left(r_1^y\right)^2 n_1^z}{\left(r_1^x\right)^2 r_1^z \left(n_1^y\right)^2 - 2r_1^x r_1^y r_1^z n_1^x n_1^y + \left(r_1^y\right)^2 r_1^z \left(n_1^x\right)^2 + \left(r_1^z\right)^3 \left(n_1^y\right)^2 - 2r_1^y \left(r_1^z\right)^2 n_1^y n_1^z + \left(r_1^y\right)^2 r_1^z \left(n_1^z\right)^2 + \left(r_1^x\right)^2 r_1^z \left(n_1^z\right)^2 - 2r_1^x \left(r_1^z\right)^2 n_1^x n_1^z + \left(r_1^z\right)^3 \left(n_1^x\right)^2}\right) + \right. \\ \qquad \left. + atan\left(\dfrac{r_1^z\left(n_1^x\right)^2 - r_1^x n_1^x n_1^z - r_1^y n_1^y n_1^z + r_1^z\left(n_1^y\right)^2}{\left(r_1^x\right)^2\left(n_1^y\right)^2 n_1^z - 2r_1^x r_1^y n_1^x n_1^y n_1^z + \left(r_1^y\right)^2\left(n_1^x\right)^2 n_1^z + \left(r_1^z\right)^2\left(n_1^y\right)^2 n_1^z - 2r_1^y r_1^z n_1^y \left(n_1^z\right)^2 + \left(r_1^y\right)^2\left(n_1^z\right)^3 + \left(r_1^x\right)^2\left(n_1^z\right)^3 - 2r_1^x r_1^z n_1^x\left(n_1^z\right)^2 + \left(r_1^z\right)^2\left(n_1^x\right)^2 n_1^z}\right)\right] < 1 \\ \left(r_1^x\right)^2 + \left(r_1^y\right)^2 + \left(r_1^z\right)^2 = 1 \end{cases} \tag{35}$$

$$\overrightarrow{r}_k = \begin{pmatrix} \sin(\theta_k)o_{k-1}^x - \cos(\theta_k)o_{k-1}^y \\ \sin(\theta_k)u_{k-1}^x - \cos(\theta_k)u_{k-1}^y \\ \sin(\theta_k)s_{k-1}^x - \cos(\theta_k)s_{k-1}^y \end{pmatrix}, \quad \text{with} : \theta_k$$
$$= asin\left\{\left(\frac{v_k}{v_1}\right)\cdot\sin\left[\theta_1 + atan\left(\frac{n_1^{x'}}{n_1^{y'}}\right)\right]\right\} - atan\left(\frac{n_{k-1}^{x'}}{n_{k-1}^{y'}}\right) \tag{33}$$

Therefore, the coordinates $\left(P_i^x, P_i^y\right)$ of the incidence points, from the 2nd to the $(k-1)^{\text{th}}$ incidence points, are the solution of the system with the equation of the line for the source P_{i-1}, whose direction is given by the unitary vector $(\overrightarrow{\boldsymbol{r}}_i)$, and the equation relative to the i^{th} interface, $z = f_i(x,y)$. This system of equations is given in Appendix A. Finally, the coordinates $\left(T_0^x, T_0^y, T_0^z\right)$ of the resulting target point related to the initial guess angle θ_1 (given as input), are the solution of the system containing the equation of the line for the point P_{k-1} and the horizontal plane for T ($z = T^z$), as shown given in Appendix B.

Thus, the bisection method is applied to the two error functions,

Isolating the ratios r_1^x/r_1^z and r_1^y/r_1^z from the first two inequalities and expressing r_1^z as a function of such ratios, from the unitary modulus condition, leads to obtaining the lower and upper domain interval values for the components of $\overrightarrow{\boldsymbol{r}}_1$, which are respectively a^x, a^y, a^z and b^x, b^y and b^z, as given in (37).

It is clear that the extremities of the interval depend on the incidence point at the first interface, since the partial derivatives of the first interface function, $\frac{\partial f_1}{\partial x}(x,y)$ and $\frac{\partial f_1}{\partial y}(x,y)$, are computed for $(x,y) = \left(P_1^x, P_1^y\right)$. Therefore, the choice of the initial guess for P_1 is critical to ensure the convergence to the root solution, through the bisection method. Following the same approach used for the two dimensional case, the intersection between the segment $\overline{ST}$ and the first interface $f_1(x,y)$ is used to guide the selection of the initial guess point. Indicating with $P_0 \equiv \left(P_0^x, P_0^y, P_0^z\right)$ the intersection between $\overline{ST}$ and $f_1(x,y)$, the initial

$$\begin{cases} -1 < \left(\frac{v_i}{v_{max}}\right) \cdot sin\left[-atan\left(\frac{r_1^x}{r_1^z}\right) - atan\left(\frac{\partial f_1}{\partial x}\left(P_1^x, P_1^y, P_1^z\right)\right)\right] \Big\langle 1 \\ -1 < \left(\frac{v_i}{v_{max}}\right) \cdot sin\left[-atan\left(\frac{r_1^y}{r_1^z}\right) - atan\left(\frac{\partial f_1}{\partial y}\left(P_1^x, P_1^y, P_1^z\right)\right)\right] \Big\langle 1 \\ \left(r_1^x\right)^2 + \left(r_1^y\right)^2 + \left(r_1^z\right)^2 = 1 \end{cases}$$

$$\begin{cases} -tan\left[asin\left(\frac{v_1}{v_{max}}\right) + atan\left(\frac{\partial f_1}{\partial x}\left(P_1^x, P_1^y, P_1^z\right)\right)\right] \Big\langle \frac{r_1^x}{r_1^z} < tan\left[asin\left(\frac{v_1}{v_{max}}\right) - atan\left(\frac{\partial f_1}{\partial x}\left(P_1^x, P_1^y, P_1^z\right)\right)\right] \\ -tan\left[asin\left(\frac{v_1}{v_{max}}\right) + atan\left(\frac{\partial f_1}{\partial y}\left(P_1^x, P_1^y, P_1^z\right)\right)\right] \Big\langle \frac{r_1^y}{r_1^z} < tan\left[asin\left(\frac{v_1}{v_{max}}\right) - atan\left(\frac{\partial f_1}{\partial y}\left(P_1^x, P_1^y, P_1^z\right)\right)\right] \\ r_1^z = -\sqrt{\frac{1}{\left(\frac{r_1^x}{r_1^z}\right)^2 + \left(\frac{r_1^y}{r_1^z}\right)^2 + 1}} \end{cases} \tag{36}$$

$$\begin{pmatrix} a^x \\ a^y \\ a^z \end{pmatrix} = \begin{pmatrix} -tan\left[asin\left(\frac{v_1}{v_{max}}\right) - atan\left(\frac{\partial f_1}{\partial x}(P_1)\right)\right] \cdot \left\{\left(tan\left[asin\left(\frac{v_1}{v_{max}}\right) - atan\left(\frac{\partial f_1}{\partial x}(P_1)\right)\right]\right)^2 + \left(tan\left[asin\left(\frac{v_1}{v_{max}}\right) - atan\left(\frac{\partial f_1}{\partial y}(P_1)\right)\right]\right)^2 + 1\right\}^{-\frac{1}{2}} \\ -tan\left[asin\left(\frac{v_1}{v_{max}}\right) - atan\left(\frac{\partial f_1}{\partial y}(P_1)\right)\right] \cdot \left\{\left(tan\left[asin\left(\frac{v_1}{v_{max}}\right) - atan\left(\frac{\partial f_1}{\partial x}(P_1)\right)\right]\right)^2 + \left(tan\left[asin\left(\frac{v_1}{v_{max}}\right) - atan\left(\frac{\partial f_1}{\partial y}(P_1)\right)\right]\right)^2 + 1\right\}^{-\frac{1}{2}} \\ -\left\{\left(tan\left[asin\left(\frac{v_1}{v_{max}}\right) - atan\left(\frac{\partial f_1}{\partial x}(P_1)\right)\right]\right)^2 + \left(tan\left[asin\left(\frac{v_1}{v_{max}}\right) - atan\left(\frac{\partial f_1}{\partial y}(P_1)\right)\right]\right)^2 + 1\right\}^{-\frac{1}{2}} \end{pmatrix}$$

$$\begin{pmatrix} b^x \\ b^y \\ b^z \end{pmatrix} = \begin{pmatrix} tan\left[asin\left(\frac{v_1}{v_{max}}\right) + atan\left(\frac{\partial f_1}{\partial x}(P_1)\right)\right] \cdot \left\{\left(tan\left[asin\left(\frac{v_1}{v_{max}}\right) + atan\left(\frac{\partial f_1}{\partial x}(P_1)\right)\right]\right)^2 + \left(tan\left[asin\left(\frac{v_1}{v_{max}}\right) + atan\left(\frac{\partial f_1}{\partial y}(P_1)\right)\right]\right)^2 + 1\right\}^{-\frac{1}{2}} \\ tan\left[asin\left(\frac{v_1}{v_{max}}\right) + atan\left(\frac{\partial f_1}{\partial y}(P_1)\right)\right] \cdot \left\{\left(tan\left[asin\left(\frac{v_1}{v_{max}}\right) + atan\left(\frac{\partial f_1}{\partial x}(P_1)\right)\right]\right)^2 + \left(tan\left[asin\left(\frac{v_1}{v_{max}}\right) + atan\left(\frac{\partial f_1}{\partial y}(P_1)\right)\right]\right)^2 + 1\right\}^{-\frac{1}{2}} \\ -\left\{\left(tan\left[asin\left(\frac{v_1}{v_{max}}\right) + atan\left(\frac{\partial f_1}{\partial x}(P_1)\right)\right]\right)^2 + \left(tan\left[asin\left(\frac{v_1}{v_{max}}\right) + atan\left(\frac{\partial f_1}{\partial y}(P_1)\right)\right]\right)^2 + 1\right\}^{-\frac{1}{2}} \end{pmatrix} \tag{37}$$

guess point is chosen as:

$$P_1 \equiv \begin{pmatrix} P_1^x \\ P_1^y \\ P_1^z \end{pmatrix} \equiv \begin{pmatrix} S^x + \frac{v_1}{v_{max}} \cdot \left(P_0^x - S^x\right) \\ S^y + \frac{v_1}{v_{max}} \cdot \left(P_0^y - S^y\right) \\ f_1\left(S^x + \frac{v_1}{v_{max}} \cdot \left(P_0^x - S^x\right), S^y + \frac{v_1}{v_{max}} \cdot \left(P_0^y - S^y\right)\right) \end{pmatrix} \tag{38}$$

Therefore, the bisection method can be applied, following the same steps as for the case with flat interfaces until convergence is satisfactory (that is, $(c^x - a^x)$, $(c^y - a^y)$, $(c^z - a^z)$ and/or $|e_x(c)|$ and $|e_y(c)|$ sufficiently small), returning $\overrightarrow{r}_1 = \langle c^x, c^y, c^z \rangle$ and stopping iterating. Fig. 5b illustrates the ray tracing relative to the initial guess for $\overrightarrow{r}_1$, the first four iterations of the method and the final solution at the target.

6. Application examples

The proposed mathematical model can be applied to several scenarios, to enable accurate ultrasound ray tracing and improve ultrasonic inspection. Multi-layered structures, such as composite parts and coated components, are becoming common in many fields, since they are appreciated for their unique mechanical properties. Also, any ultrasonic inspection performed through embedding the probe within a coupling

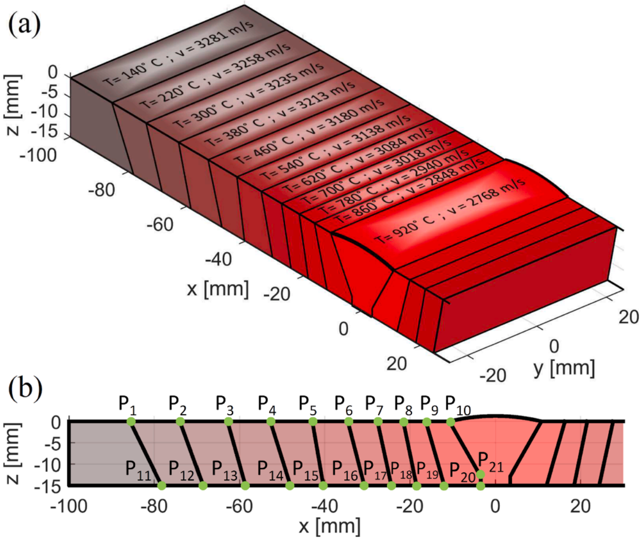

Fig. 7. (a) Discretization of welded plate through eleven regions with constant temperature and (b) transversal section with key points used for computation of analytical surfaces.

wheel, whose rubber tyre has a significant velocity mismatch with either internal or external media (i.e. designed to withstand temperatures rather than optimal acoustic matching), should be considered as a multi-layered inspection [19]. The three dimensional tracing of ultrasonic rays is often approximated in these situations, with the result of compromising the effectiveness of ultrasonic inspection techniques used to detect cracks and defects. Robotic inspection systems have been developed in recent years to speed up the inspection of large parts made of composite materials [8,20]. A robot manipulator usually moves an ultrasonic phased array probe along the contour of a surface, while pulse-echo signals are collected. However, when parts are thick and/or their thickness is variable, it is necessary to employ two manipulators, the first for holding the generating ultrasonic probe from one side of the part and the second for receiving the signal from the other side of the component respectively [21]. The presented mathematical model can be used to compute the direction of the transmitted ultrasonic ray, thus optimizing the orientation of the receiving transducer throughout the inspection of such complex geometries. The capability of the model to work in the three dimensional space makes it suitable to be used for challenging-to-inspect parts with complex geometries.

For the sake of presenting a practical application example of the model, the remaining part of this paper focuses on the field of in-process ultrasonic inspection of welded plates. Non-destructive evaluation (NDE) in the form of UT testing has become the industrial standard for welds to be tested in a safe, efficient and unobtrusive manner. Traditionally, fusion welding and NDE of welds are separate processes in the supply chain, which ultimately limit productivity, throughput and increase rework. Therefore, researchers are currently working hard to combine both of these practices directly at the point of manufacture through the use of new inspection, automation and control approaches [22–26]. The concept of inspecting the welding process in real-time offers the possibility to control, adapt and consistently ensure high-quality defect-free welding. Early detection of defects, in high-value thick complex welded components, would result in reduced rework requirements and hence improved component build time and overall cost. Inspection of each pass during the welding process would allow the early and efficient screening of each layer and detection of any flaws [23]. However, ultrasonic inspection of the welds at the point of manufacture is challenging, due to the high temperature of the welded parts. The speed of sound in a material changes with its temperature. Javadi et al. [23] demonstrated that the ultrasonic inspection results can be considerably influenced by the temperature. For example, a defect can be located with a position mismatch of up to 3 mm in two inspections carried out at 28 °C and 164 °C. Mild steel melts at around 1370 °C. Therefore, welded parts at the point of manufacture present a temperature gradient, with temperatures rising from room temperature to several hundreds of degrees C (depending on the time elapsed from the deposit of the welding material). It is notoriously difficult to predict the path that an ultrasound ray follows from a source to a target point, when it travels through a material with non-constant temperatures. This could be computed through Finite Element Modelling (FEM), but thermo-mechanic FEM simulations are usually very resource-demanding and time-consuming. This section demonstrates how the presented mathematical model can be used to approximate the ultrasonic paths, by

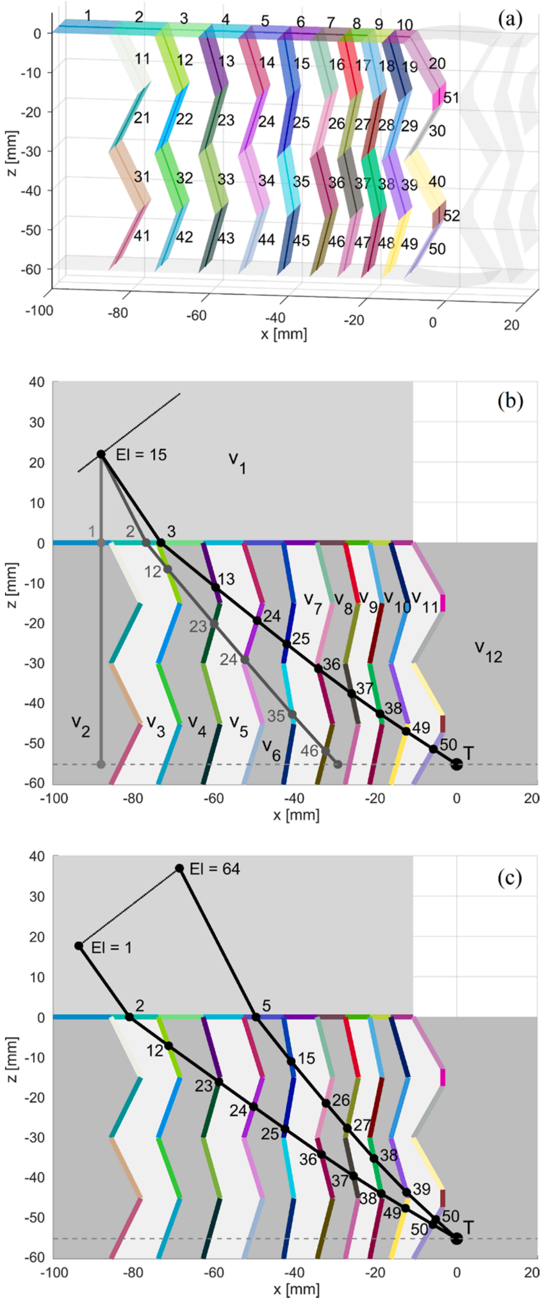

Fig. 8. (a) Three dimensional view of all analytical interfaces in the final model, (b) interfaces intersected by the rays produced with the bisection method for the 15th element of the PA probe and (c) interfaces intersected by the final rays for the 1st and the 64th element of the probe.

Table 1
Coordinates of key points of the welded sample model.

Key point coordinates [mm]						Shear velocity [m/s]	
Point	**x**	**z**	**Point**	**x**	**z**	$\mathbf{v_1}$	2340
$\mathbf{P_0}$	−150.0	0.00	$\mathbf{P_{11}}$	−78.27	−15.00	$\mathbf{v_2}$	3281
$\mathbf{P_1}$	−85.68	0.00	$\mathbf{P_{12}}$	−68.53	−15.00	$\mathbf{v_3}$	3258
$\mathbf{P_2}$	−73.98	0.00	$\mathbf{P_{13}}$	−58.62	−15.00	$\mathbf{v_4}$	3235
$\mathbf{P_3}$	−62.85	0.00	$\mathbf{P_{14}}$	−48.07	−15.00	$\mathbf{v_5}$	3213
$\mathbf{P_4}$	−52.79	0.00	$\mathbf{P_{15}}$	−40.34	−15.00	$\mathbf{v_6}$	3180
$\mathbf{P_5}$	−42.92	0.00	$\mathbf{P_{16}}$	−30.73	−15.00	$\mathbf{v_7}$	3138
$\mathbf{P_6}$	−34.59	0.00	$\mathbf{P_{17}}$	−24.37	−15.00	$\mathbf{v_8}$	3084
$\mathbf{P_7}$	−27.63	0.00	$\mathbf{P_{18}}$	−18.47	−15.00	$\mathbf{v_9}$	3018
$\mathbf{P_8}$	−21.57	0.00	$\mathbf{P_{19}}$	−12.01	−15.00	$\mathbf{v_{10}}$	2940
$\mathbf{P_9}$	−16.33	0.00	$\mathbf{P_{20}}$	−3.46	−15.00	$\mathbf{v_{11}}$	2848
$\mathbf{P_{10}}$	−10.80	0.00	$\mathbf{P_{21}}$	−3.46	−12.88	$\mathbf{v_{12}}$	2768

discretizing the material of a welded plate with a succession of constant temperature regions. Fig. 7a shows the reference case used herein. The sample under consideration is a 15 mm thick steel specimen with a 60 degrees single V-groove weld. Two mild steel 15 mm thick plates are supposed to be butt-welded and the temperature of the deposited material is supposed to have cooled for 6 min after completion of the weld process. In order to consider the thermal distribution in the weldment, and the associated spatial variation in elastic properties, a finite element (FE)-derived thermal distribution map obtained from a weld model was corroborated experimentally using thermocouple measurements [27]. The resultant map comprises eleven temperature zones across the specimen, with relative sound speed in the material, to represent the effect of temperature variation on wave propagation.

Fig. 7b gives a transversal section of such interfaces, with the key points used to express the interfaces as analytical surfaces. Although this work introduced the generalised mathematical model of Snell's law for curved material interfaces (the three dimensional case, described in Section 5), the observant reader will realize that any evolution of the temperature in the y-direction is neglected in this example. This is just for the sake of clarity, to make the example and the following figures more easily comprehensible.

The ith horizontal superficial interface at the top of the welded plate, between the points P_i and P_{i+1}, is represented analytically by the function:

$$z = f(x, y) = z_{P_i};\text{for}: \begin{cases} x_{P_i} < x < x_{P_{i+1}} \\ -\infty < y < \infty \end{cases} \tag{39}$$

The ith volumetric tilted interface, between the points P_i and P_{i+10}, is represented analytically by the function:

$$z = f(x, y) = mx + b;\text{with}: \begin{cases} m = \dfrac{z_{P_{i+10}} - z_{P_i}}{x_{P_{i+10}} - x_{P_i}} \\ b = -m^* x_{P_i} \end{cases};\text{for}: \begin{cases} x_{P_i} < x < x_{P_{i+10}} \\ -\infty < y < \infty \end{cases} \tag{40}$$

Finally, the vertical surface corresponding to the root face at the bottom of the bevel is given analytically by the following function:

$$x = f(y, z) = x_{P_{20}};\text{for}: \begin{cases} -\infty < y < \infty \\ z_{P_{20}} < z < z_{P_{21}} \end{cases} \tag{41}$$

While straight beam techniques can be highly effective at finding laminar flaws, they are not effective when testing many common welds, where discontinuities are typically not oriented parallel to the surface of the welded plates. The combination of weld geometry, the orientation of flaws, and the presence of the weld crown or bead require inspection from the side of the weld using a beam generated at an angle. Angle beam testing is by far the most commonly used technique in ultrasonic flaw detection in butt welds [28–30]. Angle beam probes consist of a transducer and a wedge. They use the principle of refraction and mode conversion at a boundary to produce refracted shear waves in the test piece [31,32]. When using wide phased array probes, the wedge can be quite bulky and impede the generation of shear waves close to the edge of the weld crown. For this reason, the ultrasound waves arrive to the region to inspect after a single or double bounce at the back wall of the part, respectively known as V-transmission and W-transmission [32]. This work considers the case of the W-transmission, since this is the case

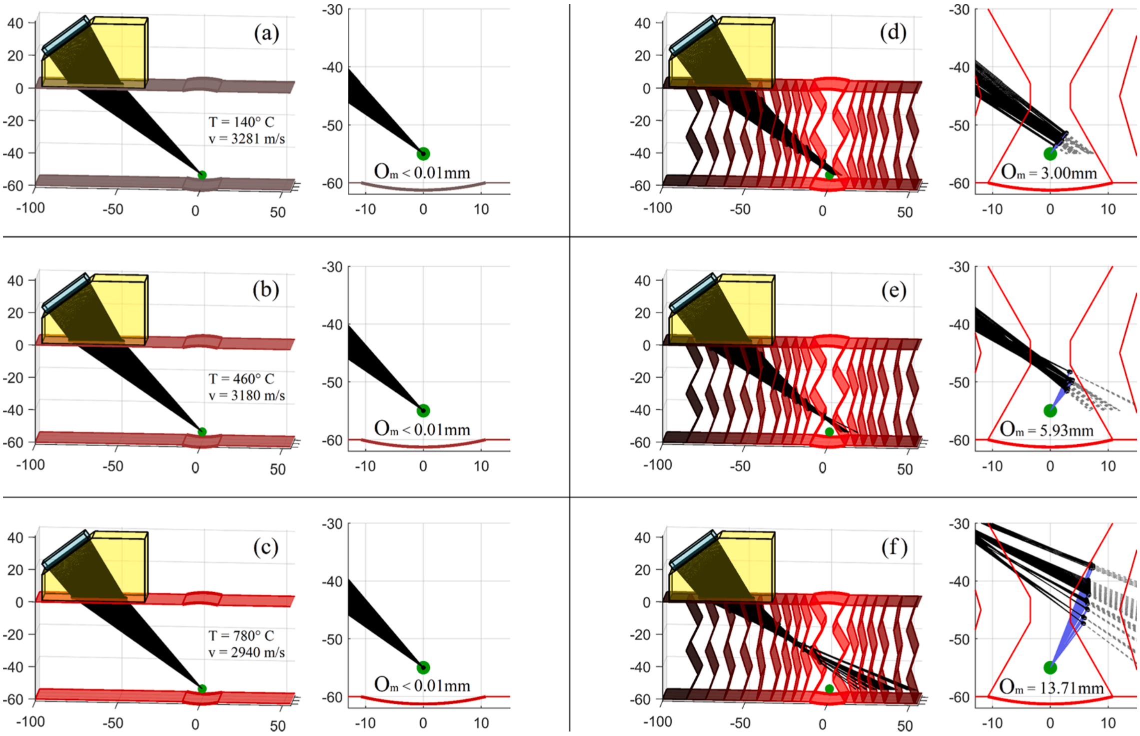

Fig. 9. Ray tracing from all PA sources to the target point assuming constant temperatures of 140 °C (a), 460 °C (b) and 780 °C (c) for the welded plate. Propagation of the resulting incidence vectors to the reference model with multiple regions separated by interface surfaces (d, e and f).

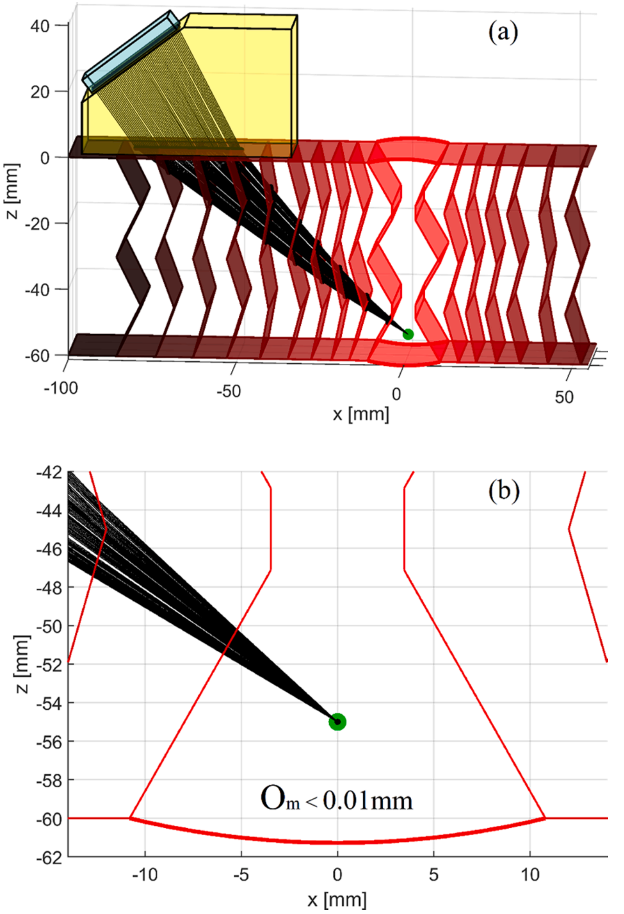

Fig. 10. Ray tracing from all phased array sources to the target point in the reference sample (a) and close up image of the area around the target (b).

where the ultrasonic waves travel more distance. Pettigrew et al. demonstrated that it is acceptable and convenient to interpret the data obtained from reflected ultrasonic waves in mirrored schematic representation [33]. Therefore, for the preparation of this inspection mode and for the interpretation of its results, it is common practice to illustrate the propagation of the shear ultrasonic rays in a schematic representation obtained through mirroring the geometry (in Fig. 7) twice, with respect to the bottom plane, and appending the resulting mirrored copies to the bottom of the original geometry. The result of this operation is shown in Fig. 8.

The final model contains 52 interface surfaces. The horizontal superficial interfaces at the top of the welded plate, analytically defined by Eq. (41), are indexed with the numbers from 1 to 10. The remaining surfaces with indices from 11 to 20 and the root face indexed with the number 51, respectively defined by Eqs. (42) and (43), are mirrored twice with respect to the x-y plane and translated vertically, producing the analytical surfaces indexed with the numbers from 21 to 50 and 52. Fig. 8a shows a three dimensional view of the final model, where each analytical surface is plotted with its given index and with a different colour, to ease the individuation of all surfaces. Fig. 8b shows a side view of the representation and illustrates how the surfaces intersected by the ultrasonic rays, computed through the iterations of the generalised bisection method, can be different for each ray. The same applies to the final rays (originating from the convergence of the method), as shown in Fig. 8c. The indices of the intersected surfaces are reported next to the relative intersection points. This work assumes the use of a 64 element 0.5 mm pitch 5 MHz PA probe, mounted on a wedge with a nominal incidence angle of 37.6°. The centre of the first element of the array is located at $x = -93.65$ mm and $z = 17.68$ mm. The target (T) is located at $x = 0.00$ mm and $z = -55.00$ mm. It is assumed that the in-process inspection of the weld is executed by bringing the wedge into contact with the surface of the hot plate only for few seconds, the time required to trigger the elements of the probe and receive the returning ultrasonic echoes. For this assumption, the heat transfer between the wedge material and the plate is neglected. The wedge temperature is assumed to stay constant and the temperatures of the plate regions to be unaffected by the contact with the wedge. Table 1 gives the coordinates of all key

Table 2
Computation times.

Temperature of model used for computation	Num. of interfaces	Num. rays	Average num. of iterations	Average duration of each iteration [ms]	Average convergence time per ray [s]	Total elapsed time [s]
Constant (140 °C)	1	64	13.20	3.98	0.0527	3.38 s
Constant (460 °C)	1	64	13.51	3.87	0.0523	3.35 s
Constant (780 °C)	1	64	13.45	3.91	0.0526	3.36 s
2 zones	7	64	13.64	21.86	0.2982	19.08 s
4 zones	17	64	13.83	96.14	1.3295	85.09 s
6 zones	27	64	13.98	230.65	3.2255	206.43 s
8 zones	37	64	15.67	449.48	7.0443	450.83 s
10 zones	47	64	14.91	759.96	11.3281	725.00 s
Ref. model (11 zones)	52	64	14.95	960.36	14.3603	919.06 s

Table 3
Distances and transit times (absolute and relative).

	Absolute travel distance and time				Evaluation in reference model with 11 zones			
Temperature of model used for computation	Min transit distance [mm]	Max transit distance [mm]	Min transit time [μs]	Max transit time [μs]	Mean distance from target (O_m) [mm]	Max distance from target [mm]	Mean shift in transit time [μs]	Max shift in transit time [μs]
Constant (140 °C)	115.4547	119.5808	39.1287	40.3255	2.9995	4.5881	1.5774	2.4261
Constant (460 °C)	115.3408	119.4464	40.0723	41.0339	5.9310	7.5542	3.4099	5.5051
Constant (780 °C)	115.0820	119.1156	42.4144	42.8997	13.7115	19.2990	9.3275	17.4573
2 zones	114.9971	118.9979	43.4097	43.7610	16.8022	25.4787	11.8421	25.5825
4 zones	115.4540	119.7607	41.5273	42.9150	3.9199	5.9205	1.8740	2.8408
6 zones	115.6486	119.8180	41.1850	42.6217	1.4377	2.1348	0.6899	1.1720
8 zones	115.6218	119.7808	41.0746	42.5057	1.1135	2.6651	0.5349	1.2874
10 zones	115.8426	119.7384	41.0016	42.4173	0.7981	2.1470	0.3735	0.7879
Ref. model (11 zones)	115.7414	119.7349	40.9628	42.3805	0.0028	0.0062	null	null

points shown in Fig. 7b and the shear velocities indicated in Fig. 8b. Whereas the shear velocity in the wedge is indicated with v_1, the shear velocities in the welded plate regions are specified with v_2, v_3, …, and v_{12}.

Due to the limited size of the horizontal interfaces and the high tilt of the volumetric interfaces, each ultrasonic ray intersects a different subset of interface surfaces, as indicated above and shown in Fig. 8b and c. Therefore, the introduced generalization of the bisection method, described in Section 5, has been refined to cope with this additional challenge. For every refraction, the analytic equation of the line for the last intersection point, whose direction is given by the unitary refraction vector ($\overrightarrow{r}$), is intersected in turn with all the analytic functions of the interfaces. This operation gives one intersection point for each interface surface. The interface that produces the closest point to the last intersection point is selected as the correct intersection surface and the point is returned as the location where a new refraction takes place. This continues until the horizontal plane for the target (T) is reached.

The generalized bisection method was first used to compute the ray tracing for three easy cases, assuming a constant temperature of 140 °C, 460 °C and 780 °C (see Fig. 9a-c). Respectively, shear velocities of 3281, 3180 and 2940 m/s were used for the whole welded plate, for the three cases. Obtaining a distance from target smaller than 0.01 mm has been used as stopping criterion in our work, to stop the iterations of the bisection method. Note, the stopping criterion can be different, depending on the application. In practical applications of the method, a meaningful approach would be to stop iterating when the change in transit time is smaller than a defined fraction of a wavelength. Then, the resulting incidence vectors for the PA sources were propagated through the interface surfaces of the reference model with multiple temperature (see Fig. 9d-f). This demonstrates that, when assuming constant temperature for the welded plate, accurate ultrasonic focusing can be seriously compromised in in-process inspection scenarios. Indicating with O_m the average minimum distance between the target point and the ultrasonic rays, the propagation of the incidence vectors produces, for the three cases, average distances equal to 3.00, 5.93 and 13.71 mm.

The introduced bisection method was applied to the reference model, considering all its 52 interface surfaces, to find the optimum incidence angle for all the ultrasonic rays originating from the phased array elements, in order to focus the ultrasonic waves at the target. As for the constant temperature cases, here also, the iterations of the bisection method were stopped at errors smaller than 0.01 mm. Fig. 10 gives evidence of the result. The method enabled the accurate computation of the PA rays to achieve optimum focusing at the target. The generalised bisection method was implemented in Matlab 2020b and tested in a computer with an Intel® i7-6820HQ CPU (2.70 GHz, 4 Cores) and 32 Gb of Random-Access Memory. Table 2 reports quantitative performance results for the execution of the generalized bisection method in the constant temperature models and in the variable temperature model, in terms of average number of iterations, average duration of each iteration, average convergence time per each ray and total elapsed. Table 3 reports the minimum and maximum travel times and distances for each test case and the relative errors, in terms of resulting mean and maximum distances from target and shift in ultrasonic ray travel time. As expected the iterative method converges in less than 4 s when a constant temperature is assumed for the whole welded plate, since only one interface is present in this case (the interface between the wedge and the plate). However, the assumption of constant temperature causes distances as large as 19.3 mm between the ultrasonic rays and the target point and shifts in travel time as big as 17.5 μs. The maximum distance is kept below 0.01 mm, when the bisection method is applied to the full reference model with 11 temperature zones and 52 interface surfaces. In this case, the computation converges in 15 min and 19 s. In order to investigate the relationship between the computation time and the number of interfaces, additional tests were carried out interpolating the discrete temperature zones in the model, in order to generate five additional test models with 2, 4, 6, 8 and 10 zones and 7, 17, 27, 37 and 47 interfaces respectively. The resulting elapsed times in Table 2 show a quadratic dependence between the computation time of the current method and the number of surfaces in the model.

Although the method has not been optimized for speed so far and more sophisticated implementations can minimize the execution time in the future, the current result is already a great advantage if compared to the time required by Finite Element models, which is in the order of few days, to perform ray tracing for the scenario examined in this work. Nevertheless, the proposed approach can be used to pre-calculate a number of focal laws for the geometry, but with differing temperature profiles. During the inspection, temperature sensors can be used to select the most appropriate match for the thermal profile.

7. Conclusions

Ultrasonic testing is still a hot research topic. The desire to apply ultrasonic testing to geometrically complex structures, and to anisotropic, inhomogeneous materials, together with the advent of more powerful electronics and software, is constantly pushing the applicability of ultrasonic ways to their limits. General ray tracing models are currently required, to support the development of new imaging techniques, such as Full Matrix Capture and Total Focusing Method, and the execution of challenging inspections. One existing solution is to implement the Fast-Marching Method (FMM) combined with Fermat's principle and Dijkstra's algorithm. This paper introduced a generalized iterative method for the computation of ultrasonic ray paths, when ultrasonic source and target are separated by multiple complex material interfaces in the two dimensional and three dimensional domains. The method was implemented in Matlab 2020b. Starting from a review of the well-known bisection method, this work extends the applicability of the method to cases with increasing complexity and to the three dimensional domain. An application example, in the field of in-process weld inspection, was presented. The generalised bisection method enabled the computation of optimum incidence angles to achieve accurate ultrasonic focusing, through a 64-element phased array probe mounted on a wedge and a model with 52 interface surfaces. The maximum distance between the ultrasonic rays and the target is kept below 0.01 mm and the computation converged in slightly more than 15 minutes (919.06 s). Although the implementation of the method was not optimized for speed, the current result is already a great advantage if compared to the time required by Finite Element models. Future work will focus on generating more sophisticated implementations of the method, capable of minimizing the execution time without compromising the accuracy.

Declaration of Competing Interest

The authors declare that they have no known competing financial interests or personal relationships that could have appeared to influence the work reported in this paper.

Acknowledgements

This work has received funding from the European Union's Horizon 2020 research and innovation programme under the Marie Sklodowska-Curie grant agreement No 835846. Furthermore, the authors would like to thank Dr Zhen Qiu (University of Strathclyde) for providing the temperature field data of the butt-welded plates, which derived from work done for the project EP/R004889/1 - Delivering Enhanced Through-Life Nuclear Asset Management (funded by the ANRC 12-1 call on Advanced Ultrasonic Inspection and Monitoring for Challenging Industrial Welding Applications).

Appendix A

System with the equation of the line for the source P_{i-1}, whose direction is given by the unitary vector ($\vec{r}_i$), and the equation relative to the i^{th} interface, $z = f_i(x,y)$. The solution of this system leads to the coordinates $\left(P_i^x, P_i^y\right)$ of the incidence points, from the 2nd to the $(k-1)^{\text{th}}$ incidence points.

if $\left(r_i^x \neq 0, r_i^y \neq 0, r_i^z \neq 0\right)$

$$\begin{cases} line\ \ for\ \ P_{i-1}: \begin{cases} \dfrac{x-P_{i-1}^x}{r_i^x} = \dfrac{y-P_{i-1}^y}{r_i^y} \\ \\ \dfrac{y-P_{i-1}^y}{r_i^y} = \dfrac{z-P_{i-1}^z}{r_i^z} \end{cases} \\ \\ \qquad i^{th}\ \ interface: z = f_i(x,y) \end{cases}$$

elseif $\left(r_i^x = 0, r_i^y \neq 0, r_i^z \neq 0\right)$

$$\begin{cases} line\ \ for\ \ P_{i-1}: \begin{cases} x = P_{i-1}^x \\ \\ \dfrac{y-P_{i-1}^y}{r_i^y} = \dfrac{z-P_{i-1}^z}{r_i^z} \end{cases} \\ \\ \qquad i^{th}\ \ interface: z = f_i(x,y) \end{cases}$$

elseif $\left(r_i^x \neq 0, r_i^y = 0, r_i^z \neq 0\right)$

$$\begin{cases} line\ \ for\ \ P_{i-1}: \begin{cases} y = P_{i-1}^y \\ \\ \dfrac{x-P_{i-1}^x}{r_i^x} = \dfrac{z-P_{i-1}^z}{r_i^y} \end{cases} \\ \\ \qquad i^{th}\ \ interface: z = f_i(x,y) \end{cases}$$

elseif $\left(r_i^x \neq 0, r_i^y \neq 0, r_i^z = 0\right)$

$$\begin{cases} line\ \ for\ \ P_{i-1}: \begin{cases} z = P_{i-1}^z \\ \\ \dfrac{x-P_{i-1}^x}{r_i^x} = \dfrac{y-P_{i-1}^y}{r_i^y} \end{cases} \\ \\ \qquad i^{th}\ \ interface: z = f_i(x,y) \end{cases}$$

elseif $\left(r_i^x = 0, r_i^y = 0, r_i^z \neq 0\right)$

$$\begin{cases} line\ \ for\ \ P_{i-1}: \begin{cases} x = P_{i-1}^x \\ y = P_{i-1}^y \end{cases} \\ i^{th}\ \ interface: z = f_i(x,y) \end{cases}$$

elseif $\left(r_i^x = 0, r_i^y \neq 0, r_i^z = 0\right)$

$$\begin{cases} line\ \ for\ \ P_{i-1}: \begin{cases} x = P_{i-1}^x \\ z = P_{i-1}^z \end{cases} \\ i^{th}\ \ interface: z = f_i(x,y) \end{cases}$$

elseif $\left(r_i^x \neq 0, r_i^y = 0, r_i^z = 0\right)$

$$\begin{cases} line\ \ for\ \ P_{i-1}: \begin{cases} y = P_{i-1}^y \\ z = P_{i-1}^z \end{cases} \\ i^{th}\ \ interface: z = f_i(x,y) \end{cases}$$

end

Appendix B

System containing the equation of the line for the point P_{k-1} and the horizontal plane for T ($z = T^z$). The solution of this system leads to the coordinates $\left(T_0^x, T_0^y, T_0^z\right)$ of the resulting target point, related to the initial guess angle θ_1 (given as input).

if $\left(r_i^x \neq 0, r_i^y \neq 0, r_i^z \neq 0\right)$

$$\begin{cases} line\ \ for\ \ P_{i-1}: \begin{cases} \dfrac{x-P_{i-1}^{x}}{r_i^{x}} = \dfrac{y-P_{i-1}^{y}}{r_i^{y}} \\ \\ \dfrac{y-P_{i-1}^{y}}{r_i^{y}} = \dfrac{z-P_{i-1}^{z}}{r_i^{z}} \end{cases} \\ \qquad horiz.plane\ \ for\ \ T: z = T^{z} \end{cases}$$

elseif $\left(r_i^x = 0, r_i^y \neq 0, r_i^z \neq 0\right)$

$$\begin{cases} line\ \ for\ \ P_{i-1}: \begin{cases} x = P_{i-1}^{x} \\ \\ \dfrac{y-P_{i-1}^{y}}{r_i^{y}} = \dfrac{z-P_{i-1}^{z}}{r_i^{z}} \end{cases} \\ \qquad horiz.plane\ \ for\ \ T: z = T^{z} \end{cases}$$

elseif $\left(r_i^x \neq 0, r_i^y = 0, r_i^z \neq 0\right)$

$$\begin{cases} line\ \ for\ \ P_{i-1}: \begin{cases} y = P_{i-1}^{y} \\ \\ \dfrac{x-P_{i-1}^{x}}{r_i^{x}} = \dfrac{z-P_{i-1}^{z}}{r_i^{y}} \end{cases} \\ \qquad horiz.plane\ \ for\ \ T: z = T^{z} \end{cases}$$

elseif $\left(r_i^x \neq 0, r_i^y \neq 0, r_i^z = 0\right)$

$$\begin{cases} line\ \ for\ \ P_{i-1}: \begin{cases} z = P_{i-1}^{z} \\ \\ \dfrac{x-P_{i-1}^{x}}{r_i^{x}} = \dfrac{y-P_{i-1}^{y}}{r_i^{y}} \end{cases} \\ \qquad horiz.plane\ \ for\ \ T: z = T^{z} \end{cases}$$

elseif $\left(r_i^x = 0, r_i^y = 0, r_i^z \neq 0\right)$

$$\begin{cases} line\ \ for\ \ P_{i-1}: \begin{cases} x = P_{i-1}^{x} \\ y = P_{i-1}^{y} \end{cases} \\ horiz.plane\ \ for\ \ T: z = T^{z} \end{cases}$$

elseif $\left(r_i^x = 0, r_i^y \neq 0, r_i^z = 0\right)$

$$\begin{cases} line\ \ for\ \ P_{i-1}: \begin{cases} x = P_{i-1}^{x} \\ z = P_{i-1}^{z} \end{cases} \\ horiz.plane\ \ for\ \ T: z = T^{z} \end{cases}$$

elseif $\left(r_i^x \neq 0, r_i^y = 0, r_i^z = 0\right)$

$$\begin{cases} line\ \ for\ \ P_{i-1}: \begin{cases} y = P_{i-1}^{y} \\ z = P_{i-1}^{z} \end{cases} \\ horiz.plane\ \ for\ \ T: z = T^{z} \end{cases}$$

end

References

[1] L. Mordfin, Handbook of reference data for nondestructive testing, ASTM (2002).

[2] B.W. Drinkwater, P.D. Wilcox, Ultrasonic arrays for non-destructive evaluation: a review, NDT & e Int. 39 (7) (2006) 525–541.

[3] A.J. Hunter, B.W. Drinkwater, P.D. Wilcox, Autofocusing ultrasonic imagery for non-destructive testing and evaluation of specimens with complicated geometries, Ndt & E Int. 43 (2) (2010) 78–85.

[4] S. Mahaut, O. Roy, C. Beroni, B. Rotter, Development of phased array techniques to improve characterization of defect located in a component of complex geometry, Ultrasonics 40 (1–8) (2002) 165–169.

[5] J. Zhang, B.W. Drinkwater, P.D. Wilcox, A.J. Hunter, Defect detection using ultrasonic arrays: the multi-mode total focusing method, NDT & e Int. 43 (2) (2010) 123–133.

[6] B. Drinkwater, A. Bowler, Ultrasonic array inspection of the Clifton Suspension Bridge chain-links, Insight-Non-Destructive Testing Condition Monitor. 51 (9) (2009) 491–498.

[7] J. Russell, R. Long, D. Duxbury, P. Cawley, Development and implementation of a membrane-coupled conformable array transducer for use in the nuclear industry, Insight-Non-Destructive Testing Condition Monitor. 54 (7) (2012) 386–393.

[8] C. Mineo, S. Pierce, B. Wright, I. Cooper, P. Nicholson, PAUT inspection of complex-shaped composite materials through six DOFs robotic manipulators, Insight-Non-Destructive Testing Condition Monitor. 57 (3) (2015) 161–166.

[9] J. Zhang, B.W. Drinkwater, P.D. Wilcox, Efficient immersion imaging of components with nonplanar surfaces, IEEE Trans. Ultrasonics, ferroelectrics, Frequency Control 61 (8) (2014) 1284–1295.

[10] M. Sutcliffe, M. Weston, P. Charlton, K. Donne, B. Wright, I. Cooper, Full matrix capture with time-efficient auto-focusing of unknown geometry through dual-layered media, Insight-Non-Destructive Testing Condition Monitor. 55 (6) (2013) 297–301.

[11] J. Ye et al., Development of an ultrasonic ray model for phased array ultrasonic testing in austenitic weldments, in: 17th World Conference on Non-Destructive Testing, Shanghai, 2008, pp. 25-28.

[12] O. Nowers, D.J. Duxbury, J. Zhang, B.W. Drinkwater, Novel ray-tracing algorithms in NDE: application of Dijkstra and A* algorithms to the inspection of an anisotropic weld, NDT & E Int. 61 (2014) 58–66.

[13] K. M. M. Tant, E. Galetti, A. Mulholland, A. Curtis, and A. Gachagan, Effective grain orientation mapping of complex and locally anisotropic media for improved imaging in ultrasonic non-destructive testing, Inverse Problems in Science and Engineering, 2020, pp. 1-25.

[14] R.L. Burden, J.D. Faires, 2.1 The bisection algorithm, Numerical analysis, 1985.

[15] A. Rontó, M. Rontó, Periodic successive approximations and interval halving, Miskolc Mathematical Notes 13 (2) (2012) 459–482.

[16] A. Boultif, D. Louër, Indexing of powder diffraction patterns for low-symmetry lattices by the successive dichotomy method, J. Appl. Crystallogr. 24 (6) (1991) 987–993.

[17] A.S. Glassner, An Introduction to Ray Tracing Morgan Kaufmann, London, 1989.

[18] M. Born, E. Wolf, 1970Principles of optics, vol. 11, p. 1.

[19] C. Macleod et al., Dry-coupled automated inspection for wire+ arc additive manufacture, Review of Progress in Quantitative Nondestructive Evaluation, 2019.

[20] C. Mineo, S.G. Pierce, P.I. Nicholson, I. Cooper, Robotic path planning for non-destructive testing–A custom MATLAB toolbox approach, Robotics Computer-Integrated Manuf. 37 (2016) 1–12.

[21] C. Mineo, Automated NDT inspection for large and complex geometries of composite materials, University of Strathclyde, 2015.

[22] Y. Javadi, et al., Ultrasonic phased array inspection of a Wire+ Arc Additive Manufactured (WAAM) sample with intentionally embedded defects, Additive Manuf. 29 (2019) 100806.

[23] Y. Javadi, et al., Continuous monitoring of an intentionally-manufactured crack using an automated welding and in-process inspection system, Mater. Des. (2020) 108655.

[24] Y. Javadi, et al., Investigating the effect of residual stress on hydrogen cracking in multi-pass robotic welding through process compatible non-destructive testing, J. Manuf. Processes (2020).

[25] Y. Javadi, et al., In-process calibration of a non-destructive testing system used for in-process inspection of multi-pass welding, Mater. Des. (2020) 108981.

[26] D. Lines, et al., A flexible robotic cell for in-process inspection of multi-pass welds, Insight-Non-Destructive Testing Condition Monitor. 62 (9) (2020) 526–532, https://doi.org/10.1784/insi.2020.62.9.526.

[27] Z. Qiu et al., Study of Thermal Gradient Effect for In-Process Ultrasonic Inspection of Fusion Welding, presented at the IEEE International Ultrasonics Symposium (IUS), Glasgow (UK), 2019.

[28] Non-destructive testing of welds. Ultrasonic testing. Techniques, testing levels, and assessment, BS EN ISO 17640:2018.

[29] Non-destructive testing of welds. Ultrasonic testing. Use of automated phased array technology, BS EN ISO 13588:2019.

[30] Non-destructive testing of welds. Phased array ultrasonic testing (PAUT). Acceptance levels, BS EN ISO 19285:2017.

[31] U. Ewert et al., Performance Control: Nondestructive Testing and Reliability Evaluation, Springer Handbook of Metrology and Testing, H. Czichos, T. Saito, and L. Smith Eds. Berlin, Heidelberg: Springer Berlin Heidelberg, 2011, pp. 887-972.

[32] I. Burhan, G. Mutaiyah, D.I. Hashim, T.M. Loganathan, M.T.H. Sultan, A Guideline of Ultrasonic Inspection on Butt Welded Plates, in: IOP Conference Series: Materials Science and Engineering, vol. 554, no. 1, IOP Publishing, 2019, p. 012002.

[33] I.G. Pettigrew, D.I.A. Lines, K.J. Kirk, S. Cochran, Investigation of crack sizing using ultrasonic phased arrays with signal processing techniques, Insight-Non-Destructive Testing Condition Monitor. 48 (2) (2006).